Frangione, A.; Sánchez Salmerón, AJ.; Modica, F.; Percoco, G. (2019). Multi-step approach for automated scaling of photogrammetric micro-measurements. The International Journal of Advanced Manufacturing Technology. 102(1-4):747-757. https://doi.org/10.1007/s00170-018-03258-w

Multi-step Approach for Automated Scaling of Photogrammetric Micro-measurements

Frangione Modica Sanchez Percoco

Abstract

Photogrammetry can be used for the measurement of small objects with microfeatures, with good results, lower cost and the possible addition of texture information to the 3D models. The performance of this technique is strongly affected by the scaling method, since it retrieves a model that must be scaled after its elaboration.
In this paper a fully automated multi-step scaling system is presented, based on machine vision algorithms for retrieving blurring areas. Such method allows to find the correct scale factor for a photogrammetric micro model and is compared with the existing manual method basing on the German guideline VDI/VDE 2634, Part 3. The proposed tool improves the performance of the manual method, eliminating operator dependent procedures. The software tool is available on-line as supplementary material and represents a powerful tool to face scaling issues of micro-photogrammetric activities.

Keywords: Measurement, Micro-features, Photogrammetry, Depth from Focus, Scale, International Standards, Image Analysis.

1 Introduction

Manufacturing of micro components in several fields of industry, such Micro Electro-Mechanical System (MEMS), medical and biomedical or automotive , has pushed to a reassessment of every tasks of the production process chain from designing to inspection [1], requiring new affordable tools [2] for measuring more complex geometric features with lower costs.

Photogrammetry is a non-contact optical technique, based on the stereoscopic principle, to retrieve geometric data of physical components.
Photogrammetry is applied in several fields, depending on the distance between the camera and the object. When this distance is small micro-features can be retrieved helping studies concerning natural sciences, [3], medical applications such as surgery [2], and odontological field [5], or very few industrial research applications for the inspection of very small components[6]–[11].
Photogrammetry applied to micrometric metrology is promising to reduce time and costs and could further compete with other expensive techniques such as interferometry, confocal microscopy, etc.
In order to allow correspondences on the surface of smooth small products, the projection of laser speckle patterns can be exploited to obtain low surface height deviations[10], [12].
Moreover a very important issue for good accuracy and precision levels is calibration [6] [13] for internal and external parameters estimation. Pin-hole calibration model is valid down to narrow angles of view
Other aspect is represented by the uncertainty of the 3D reconstruction accuracy attributable to the repeatability of the photogrammetric software [14].

However, in the literature [3], [6]–[8], [15]–[25], it is stated how one of the most important problems of the photogrammetric technique is the fact that reconstructed point clouds need to be scaled correctly, due to an inherent limitation of the technique. In other words, in a photogrammetric point cloud relative distances between objects are saved but not the absolute scale.
In this paper a fully automated system based on Otsu method to retrieve Blurring area, combined with Depth from Focus method which is available in literature but manual, is presented. Such method allows to find the correct scale factor for a photogrammetric model and is compared with existing manual method adapting the German guideline VDI/VDE 2634, Part 3. The proposed system improves the performance of the manual method, eliminating operator dependent procedures.
This paper is organized as follows: in section 2, a brief literature background is presented, the approach is proposed in section 3, while the system implementation is presented in section 4 and the results compared to the manual method are shown in section 5.

2 Literature Background

Close-range photogrammetry includes methodologies still under experimentation, achieving a considerable development thanks to low cost and fast and non-invasive scanning method.
The aspects that limit the applicability of this technology, particularly in the case of sub millimeter features, are essentially the following: when high magnifications are required, the angle of view (AOV) becomes smaller and the DOF gets narrower, leading to blurred images, accuracy of calibration pattern realization- the higher the magnification, the smaller and more accurate the pattern must be, limitations of the pinhole camera model, theoretically effective under several assumptions that cannot be verified for millimeter and micro-scale applications.
One more critical aspect, rarely treated in the research literature, regards the scale of photogrammetric point clouds, since Photogrammetry retrieves a model that must be scaled after its elaboration.
Basically, using commercial software, the scale is retrieved through two procedures [26]: the first one consists in using a known distance between two markers within the images [3], [6], [15]–[25], [27], u? for meso to large- sized objects, but small measurement volumes lead to lower field of view with the following issues: (i) the markers must be smaller with increasing costs and technical problems in fabricating them (ii) blurring involves higher image areas. In these conditions, the marker detection becomes very difficult. The second one consists in placing the camera/s in known positions [23], [28] or at a known distance between each other, as well as traditional aerial Photogrammetry, where each photo is geo-mapped through GPS[5].
A hybrid Depth from Focus(DFF)-Photogrammetry method has been shown in literature [26] for measuring and computing the scale using the same photogrammetric equipment. This method is based on the identification of the focus plane, defined as the parallel plane to the sensor, positioned at a distance equal to the focus distance of the camera.
Properly designed and manufactured certificated artefacts (one micro ball bar and micro coaxial cylinders) have been measured following and adapting the German guideline VDI/VDE 2634 [29], third part to qualify the method using a reference system, considering (i) probing error in size and the sphere spacing error, using respectively the diameter of a sphere and the distance between the centers of two spheres; (ii) probing error in form and flatness measurement error, using one sphere and one plane, respectively. The spheres were manufactured by micro-electro discharge machining (μ-EDM), due to two aspects, namely: (i) high accuracy in the micro-scale and (ii) non-reflecting surfaces caused by the presence of micro-craters induced by the process. This avoided the use of pattern projection on the artefacts, allowing an easier adaptation of the standard [29]. In fact the same standard has been used in

[10], where a laser speckle is exploited to improve recognition of surface texture by the photogrammetric software. However, since the [29] requires replicating well defined ball bar arrangements which are problematic when including the laser speckle projection system, and some ball bar arrangements cannot be measured. Consequently, in [10], ISO standards are exploited in conjunction with [29] guidelines to compensate this missing position and provide a complete verification method.
The guidelines [29] require workpieces with sizes that must be comparable to the working range that must be accurately manufactured. Consequently, specifically designed workpieces were manufactured using micro-electro discharge machining (μ-EDM).
In [26] the scaling method finds the scale factor λ through the following steps, under the hypothesis to know the magnification ratio M of the camera with the considered extension tube and L the lateral size of the pixel. The method consists in (i) capturing at least one image both with high diaphragm aperture, for example f2.8, and low aperture, such as f16; (ii) consider the f2.8 image and detect focus areas and the of the focal plane manually as the middle polyline passing through focus areas; (iii) transposition of the polyline on the same pixels of f16 image; (iv) identification of at least two geometric points that lie on the polyline and measure of the distance (in pixels) between these points; (v) conversion of the distance in into millimetres through the factors L and M; (vi) input of the computed distance in millimeters to the photogrammetric software for computing the scale factor λ.
The disadvantages of this method are basically represented by operator dependency and need of very high skills, as regards points (ii), (iii), (iv) and (v). Operators work consists in detecting non blurred areas and computing the coordinates of two points on the images in these areas.

3 Materials and Methods

In the image formation process, light radiating from points on the focus plane are mapped to a point in the sensor (sharp regions), but light from a point outside the focus plane illuminates a circle of confusion. Defocus blur occurs when this circle becomes large enough to be perceived by human eyes.
In the literature automatic algorithms utilized to measure the focus level for every image pixel are usually referred to focus measure operators. Many focus measure operators, which are applied to a small local window around a pixel, have been proposed [30].
The purpose of segmentation of defocus blur is to separate blurred and non-blurred regions. In the present paper, this problem is addressed with a sharpness metric based on Local Binary Patterns (LBP). Lorenzo et al. studied the use of Local Binary Patterns (LBP) as a focus measure for autofocus applications [31].
Since the present paper deals strictly with scaling methods and no pattern projection is used, the Probing Error in Size of [29] is the most significant test to validate the scaling method proposed by the authors since the scaling method does not affect the shape of the 3D point cloud.
In the present paper the method [26], briefly exposed in the previous section, is automated (with regard to points (ii), (iii), (iv) and (v)) in a multi-step approach, for automating the scale retrieval detection of focus areas through four main steps: 1) Segmentation, 2) distance map, 3) centres detection, 4) scale bar computation.

3.1 Segmentation

The segmentation of f2.8 images is necessary to detect the areas around the focus plane of the camera (low blur), and has been implemented on a two level approach: the first level exploits the approach described in [32], the second one exploits the Otsu's segmentation [33]: the results of these levels are combined together to improve the robustness of the approach. In Figure 1 the yellow lines indicate the algorithms based on the LBP metric [32]; the red lines are the Otsu's segmentation [33]; the blue lines indicate the cross verification of the segmented pixels and the last image shows the final segmentation of the focus areas, showed in white.

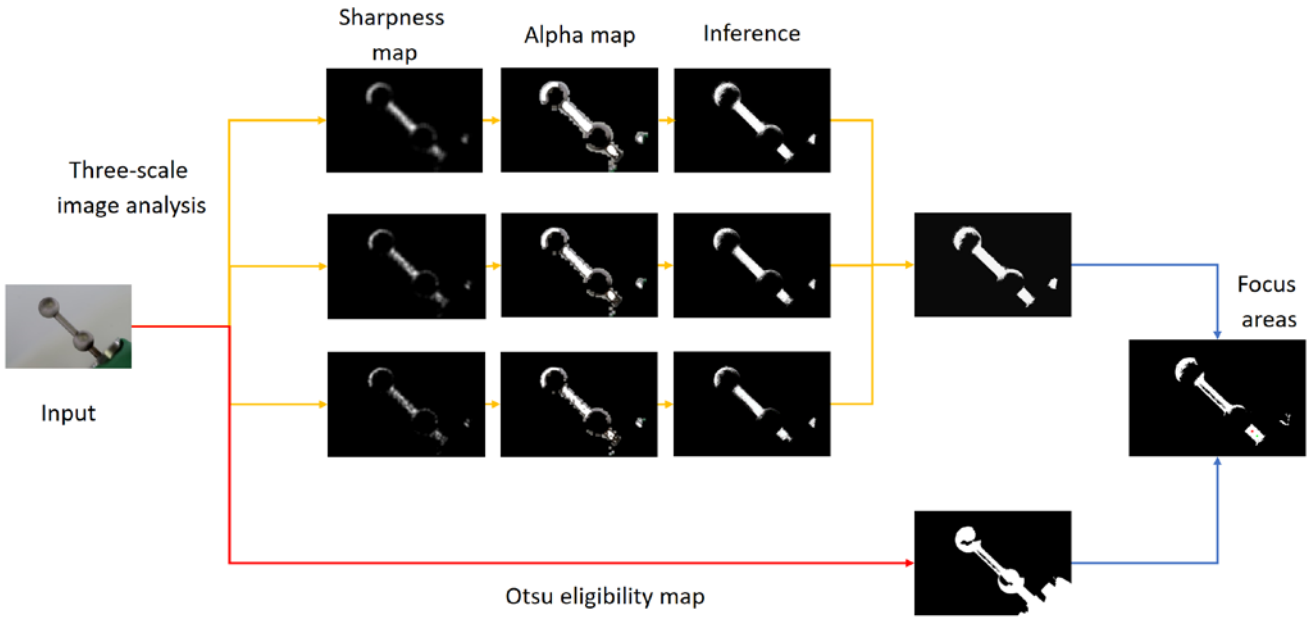

Figure 1: *Proposed approach for the automatic detection of the focus areas centres of a digital image.*

3.1.1 LBP

The first segmentation is given by a greyscale algorithm based on Local Binary Patterns (LBP) [32][34], chosen mainly for its low runtime, which allows the analysis of the entire image [35], and robustness when changes in monotonic lighting happen, frequently occurring in natural images. The approach presented in [32] and implemented in the present paper as a first level, sets up the scale value of the local patch for computing the sharpness maps equal to three different sizes of the patch (for example *11×11*, *15×15* and *21×21* pixels).

For each patch size, the computation of the LBP for each pixel (x_c, y_c) (shown in orange in Figure 2) is computed as follows:

$$LBP_{P,R}(x_c, y_c) = \sum_{p=0}^{P-1} S(n_p - n_c) \times 2^p \quad with \ S(x) = \begin{cases} 1 & |x| \geq T_{LBP} \\ 0 & |x| < T_{LBP} \end{cases} \qquad (1)$$

where P is the number of the neighbouring pixels, R is the radius of the circle with centre in the pixel (x_c, y_c) (Figure 2), n_c is the grey intensity of the pixel (x_c, y_c), n_p corresponds to the grey intensities of the pixels *P* (light blue in Figure 2) that are on the circle of radius *R; T_{LBP}>0* is a small positive threshold used to obtain a robustness higher for the analysis of the region of the smooth images [36].

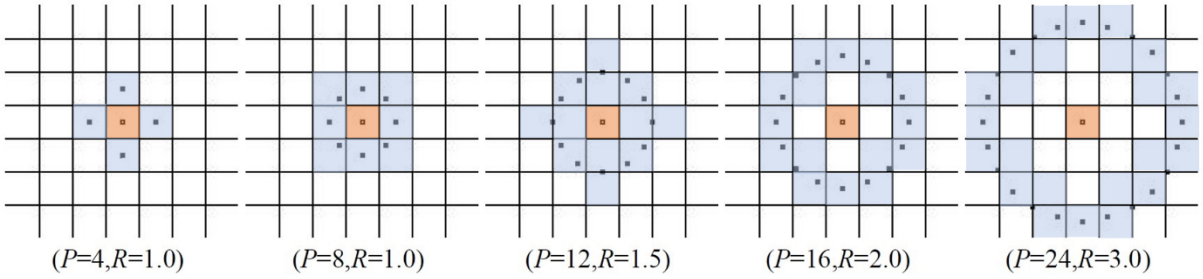

Figure 2: Examples of neighbor for several couples (P,R) [37]

The metric proposed in [32] is defined as:

$$m_{LBP} = \frac{1}{N} \sum_{i=6}^{9} n(LBP_{8,1}^{riu2} i) \qquad (2)$$

where $n(LBP_{8,1}^{riu2}i)$ is the number of rotation invariant uniform 8-bit LBP pattern of type *i*, and *N* is the total number of pixels in the selected local region to normalize the metric in order to have $m_{LBP} \in [0,1]$.
This metric is exploited to define an alpha matting initialization by applying a hysteresis threshold method with the help of two more thresholds of sharpness T_{m1} and T_{m2}. Three initial sharpness maps are assessed for three different scales and after inizialization [32], they are used as input in the Closed-Form method [38], to further extrapolate the *α-maps*. The final alpha map for each scale is denoted as α^s with s = 1, 2, 3.
The computation of the several scales is very important because if only one resolution is analyzed the result can be not correct [39]. As a consequence, in the last step of the algorithm a multi-scale graphical model [40] integrates the data belonging to each resolution. The model extracts the local blur features of the three scales and builds up an inter-scale correlation among the patches having in common the same central pixel. This correlation is expressed in form of total energy for each pixel through the equation (3) proposed in [41].
The total energy is defined as:

$$E(h) = \sum_{s=1}^{3}\sum_{i}\left|h_i^s - \hat{h}_i^s\right| + \beta\left(\sum_{s=1}^{3}\sum_{i}\sum_{j\in N_i^s}\left|h_i^s - h_j^s\right| + \sum_{s=1}^{2}\sum_{i}\left|h_i^s - h_i^{s+1}\right|\right) \quad (3)$$

where $\hat{h}_i^s = \alpha_i^s$ is the alpha map value for the scale s at pixel location i, computed through the Closed-Form method [38]; h_i^s is the sharpness value to be deducted. The first term on the right side is a unary term, which determines the cost of assigning sharpness value h_i^s to pixel *i* in the scale *s*. The second is the pairwise term enforces smoothness in the same scale and across different scales. The weight β regulates the relative importance of these two terms. For further details of the procedure used, please refer to [32].

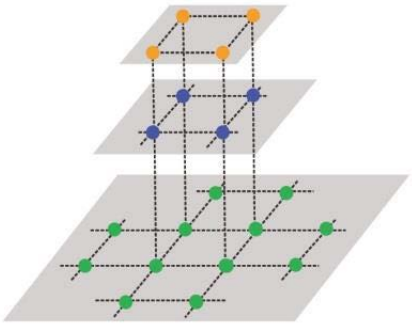

Figure 3: . Multi-scale graphical model. [40]

3.1.2 Otsu eligibility map

The authors of the present paper experienced limitations of LBP-Based [32] algorithms in sharp regions for bright objects. To overcome this drawback, one more segmentation approach has been employed, as an eligibility map I_A, where pixels belonging to the focus areas of the first segmentation I_{LBP} will be declared admissible, only if they are considered in the first foreground also in the eligibility map I_A (Fig.3):

$$I_S = I_{LBP} \cap I_A \quad (4)$$

Admissible pixels will determine the sharpness areas of the images I_S (Fig.4), from which the focus centres will be detected.

Considering that the photogrammetric scanner acquires images in a known scenario, where the background can be controlled, the well-known Otsu method [33] has been selected and employed. This method is based on bimodal histograms to binarize the greyscale image.

3.2 Distance map

After having identified the focus area of the image, the following task is to detect the centre of these areas automatically. To initialize the research of the centre, the digital image must be mapped to its *distance transform* [42], known also as *distance map* or *field of distance*. Distance maps have the capacity to label each pixel of the image, with the distance between their position and the one of the closest background pixel, that in our case will be a pixel on the edges on a binary image, belonging to the blurry areas of the final segmentation of the proposed algorithm.

3.3 Centroid detection

The manual scale approach considers the f2.8 image: the operator is asked to detect focus areas and consequently the intersection between focal plane and the object manually, being a polyline passing in the middle of focus areas. Once focus areas have been detected and segmented, at least two points belonging to the focal plane must be considered to compute the scale factor. The manual procedure asks the operator to perform this task, while the automatic approach must be provided with a criterion. The criterion exploited in the present approach is the selection of the points among the pixels with the highest probability to be in the image focus plane. The implementation has been carried out by the authors by the Euclidean distance transform.

At first a distance map, DT [42] is computed, assigning the value of the distance to the nearest blurred pixel (edge pixel, DT) to each pixel.

The detection of the first centre C1, highlighted in red in Figure 4, is done extracting the coordinates of the pixel that has the maximum distance from the edges, max [DT], i.e. the highest probability to be in the image focus plane.

The detection of the second point C2, indicated in green in Figure 4, is driven by the consideration that the distance value of this pixel from the edges DT(C2), must be included within a determined range of similarity, dependent on the distance value of the first center DT(C1). The distance value range of C2 is defined by:

$$S_{dist} * DT(C_1) \leq DT(C_2) \leq DT(C_1) \qquad (5)$$

where Sdist is the similarity coefficient [0.1,1], that multiplied to DT(C1), fixes the lower end of the range, while the upper end is given by the distance value DT(C1).

After detecting the pixels that satisfy the similarity range according to the (5), the coordinates of C2 can be computed selecting the pixel with the higher Euclidean distance from C1. Both these pixels allow to find the scale value according to [43].

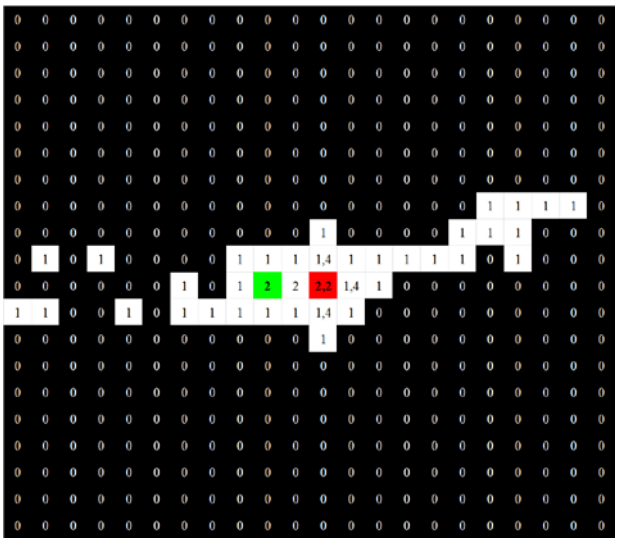

Figure 4: Detection of the focus areas centers C_1 and C_2 in the *distance map*, with S_{dist} = 0,9. The center C_1 (red) is the pixel with highest probability to be focused, with DT = 2,2; the center C_2 (green) is the pixel with DT included in the *range of similarity* and it is the furthest from the center C_1.

3.4 Scale bar computation

Subsequently it is possible to compute the euclidean distance between the centers, in [px]. As described in [43], we have:

$$1\,[pixel] = \frac{DimSen}{DimIm}[mm] \qquad (6)$$

where *DimSen* is the dimension of the camera's sensor used for the acquisition of the photo, and *DimIm* is the width of the image's resolution.
Done the conversion of the value of the distance from [px] to [mm], finally, we have that the scale bar (Figure 5) is defined as:

$$Scale\ Bar[mm] = \frac{Distance\ in\ [mm]}{IngSen} \qquad (7)$$

where *IngSen* is enlargement compared to the sensor, that depends on the dimension of the extension tube used in the phase of the acquisition of the photo [43].

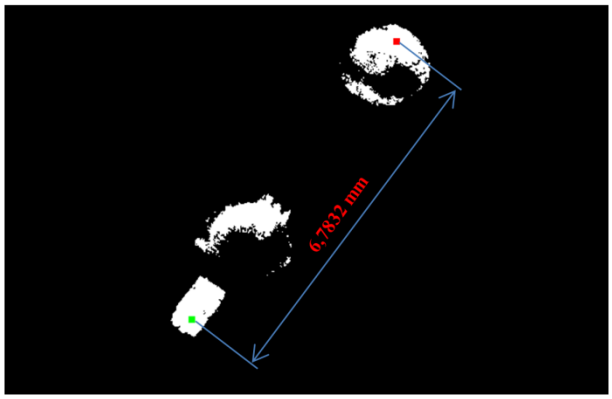

Figure 5: Scale bar in [mm] of the Ball-Bar in Fig.1.

3.5 Implementation

The system has been implemented starting from MATLAB open source codes [32][33][42], creating a Graphic User Interface (GUI), to set up useful parameters for image processing. About 9000 partially blurry images has been tested and analysed, belonging to the same set of photos as [43], on a Notebook Lenovo with 2,60 GHz Intel Core i7 and 8 GB of RAM memory. During software execution, the images are automatically resized to 640×480 pixels resolution (as suggested in [32]), then the coordinates of the identified centres in the reduced images, are normalized considering the original size (Ex.: analysing an image of resolution 3888×2952, a pixel of the resized image at the dimensions 640×480 pixels, will correspond to an area of 36,90 pixels of the original image, leading to a resizing factor equal to 6,075). The average runtime is 30,75s for each image. The acquisition method of our set images is described in [43]. The user can set up the value of sharpness thresholds T_{LBP} of equation (1), the weight β of equation (3) and the coefficient of similarity S_{dist} in equation (5), and the value of the camera sensor size, *DimSen* (6) and the enlargement compared to the sensor *IngSen* (7).

The GUI interface allows the user to select, analyse, and save one or more digital images, visualize segmented images, centres coordinates and distance values among them (Figure 6).

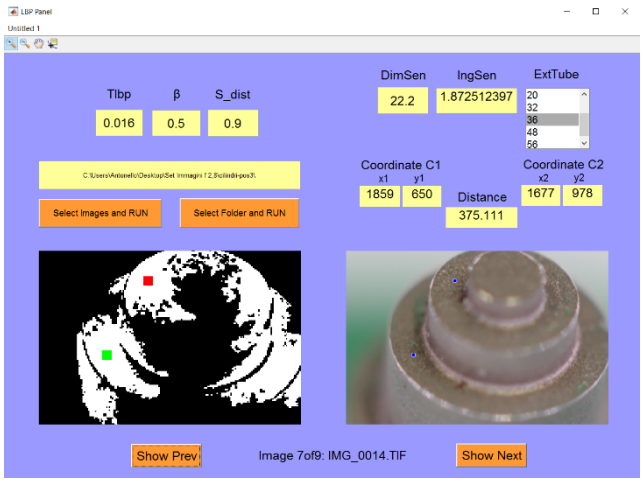

Figure 6: Visualization of the results. On the left of the MATLAB user interface, it is possible to see the zoomed image of the segmentation and the respective centers of the focus areas. On the right it is possible to see the original image with the correspondent centers, them coordinates and the value of the distance among them in pixel. Below the images there are two bottoms, useful to the navigation among the results and the information on the processed images and on the name of the current image.

The output of the software is: a cartel file, that includes the centres coordinates of each elaborated image together with the scale bar; an xml file, including name and centres coordinates of the image, belonging to the set of the analysed photo, that has the highest scale bar. The xml file is ready to be imported into the software *Agisoft PhotoScan Pro*, for the point cloud elaboration of the object.

4 Results

The evaluation the performance of the proposed approach has been based on a comparison to the manual scale method [43], analysing the same set of images representing three objects with different geometry: two spheres connected by a cylindrical bar (Ball-Bar)(Tab.1), a workpiece composed of four coaxial cylinders (Tab. 2). To validate the measurements, an adaptaion of the *VDI/VDE 2634* [29] has been followed as in [43], capturing images of the object with *f20* and *f2.8*, exploiting two different depth of focus. Each set of images included 36/72 photos of the object, which has been rotated by 5°/10° for the acquisition, an a support connected to an engine step by step. The object has been positioned on the support with a different inclination for each set [29][43].

The photogrammetric system employs a Canon EOS 400D SLR Camera with macro lens Canon EF - S 60mm f / 2.8 mounted on a tripod stand. The camera has a resolution of 10.1 megapixels (3888 x 2592), with an aspect ratio of 3: 2 while the sensor size is 22.2 mm x 14.8 mm. This camera is also equipped with a 36 mm extension tube to increase the magnification ratio. Unlike the additional lenses, extension tubes do not change the lens optical system and allow low working distances if compared to zoom lenses. On the other hand, they reduce the depth of focus and need more light intensity. This and other extension tubes on the same camera have already been studied in [6].

Tab.1: Diameters and distance center-center of the Ball-Bar [43].

Certified sizes of the Ball bar (mm)	
S1	2.0100
S2	2.0140
S1-S2	4.4990

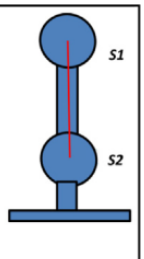

Tab.2: Certified diameters and heights of the coaxial cylinders [43].

Certified sizes of the Coaxial Cylinders (mm)	
D1	1.006
D2	2.010
D3	3.004
D4	4.003
H1	0.450
H2	0.748
H3	1.479
H4	3.004

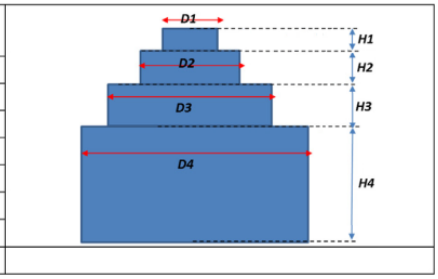

The following errors have been computed, as defined in [29]: Sphere Spacing Error (SSE), Probing Error in Size (PES), Flatness measurement error (F), Unidirectional Plane Spacing Error (UPSE).

The automatically generated *.xml*, is imported into *Agisoft PhotoScan Pro* to compute the scale bar, allowing to scale the 3D-points clouds of the object. The post-elaboration phase has been performed using the *Geomagic Studio* software where, by removing 0,3% of the noise points, *best-fit* features have been fitted on the spheres and on the cylinders of the 3D-points clouds of the analysed object similarly to [43].

After an initial trial and phase, analysing the measurements and comparing to the certified dimensions [43] of the Ball-Bar in Tab.2 and of the coaxial cylinders in Tab.1, the near optimal configurations of the parameters for the three analysed objects has been set as:

$$Ball\text{-}Bar: [T_{LBP} = 0.016; S_{dist} = 0.9; \beta = 0.5]$$

$$Coaxial\ Cylinders: [T_{LBP} = 0.032; S_{dist} = 0.9; \beta = 0.5]$$

Discussion of results

Data in Tab. 3 show the measurements of the diameters and spheres *S1* e *S2* and the distance between them centers, the certified dimensions and the results of the manual scale method. It is possible to see that, for each measurements, the diameter of *S2* is always higher than *S1*, also the standard deviations denote a good stability of *S1* and *S2* measurements (respectively *4,1μm* and *4,7μm*). The standard deviation of the distance, is equal to *12μm* and because it depends on the previous errors, it can be considered acceptable. The worse measurements come from the position 6 of the *SUT*, that can be identified in the lowest number of points.

Tab.3: Results and comparisons of the measures among the 3D-points clouds of the Ball-Bar, the certified measures and the manual scale method.

SUT	pos 1	pos 2	pos 3	pos 4	pos 5	pos 6	pos 7	Average	Certified [43]	Manual [43]
S1 Diameter [mm]	1,9993	2,0024	2,0071	1,9990	2,0048	1,9953	1,9984	2,0009	2,0100	1,9981
S2 Diameter [mm]	2,0096	2,0074	2,0112	2,0020	2,0104	1,9994	2,0108	2,0073	2,0140	2,0039
Distance S1-S2 [mm]	4,4975	4,5057	4,5115	4,5025	4,5057	4,4744	4,4987	4,4994	4,4990	4,4899
Number of points	235424	236316	235295	214341	204781	187668	232439	220895		215399

Tab.4: Measurement errors of the Ball-Bar with respect to the certified dimension and comparison with the errors given by the manual scale method.

Errors [μm]	pos 1	pos 2	pos 3	pos 4	pos 5	pos 6	pos 7	Average	Std. Dev.	ABS MAX	Av. Manual [43]
PES S1	-10,7	-7,6	-2,9	-11,0	-5,2	-14,7	-11,6	-9,1	4,1	14,7	-11,9
PES S2	-4,4	-6,6	-2,8	-12,0	-3,6	-14,6	-3,2	-6,7	4,7	14,6	-10,1
SSE	-1,5	6,7	12,5	3,5	6,7	-24,6	-0,3	0,4	12,0	24,6	-9,1

In Tab. 4 the measurements errors of our automatic scale method have been compared, with respect to the certified dimensions, with the errors of the manual method. It is evident as our method is more sensible, considering that it improves all the estimates and it decreases of *2,8μm* the *Probing Errors in Size (PES)* of *S1* and of *3,4μm* the *PES* of *S2*. Note that the result of the *Sphere Spacing Error (SSE)* decreases of *8,7μm*, and it is equal to *0,4μm*.
In Tab. 4 and 5 it is possible to analyse the data regarding the diameters and the heights of the coaxial cylinders, the *PSE*, concerning the estimation of the cylinders diameters errors and the *Unidirectional Plane Spacing Error (UPSE)*. In some positions of the *cylinders 1*, *2* and *3*, it is impossible to do measurements, given that not been able to extrapolate the 3D-points clouds.

Tab.4: Results related to the 3D-points clouds of the coaxial cylinders (ND is the impossibility of elaboration of the 3D-points clouds from the software).

SUT	pos 1	pos 2	pos 3	pos 4	pos 5	pos 6	pos 7	Average	Certified [43]	Manual [43]
D1 [mm]	1,0106	1,0063	1,0095	1,0042	ND	1,0067	1,0061	1,0072	1,0060	1,0035
D2 [mm]	2,0073	2,0068	2,0092	ND	ND	2,0048	ND	2,0070	2,0100	2,0027
D3 [mm]	3,0037	3,0035	3,0044	ND	ND	3,0014	3,0034	3,0033	3,0040	3,0021
D4 [mm]	4,0028	4,0070	4,0036	4,0069	3,9792	4,0020	4,0019	4,0005	4,0030	4,0039
H1 [mm]	0,4481	0,4498	0,4490	0,4461	0,4481	0,4479	0,4491	0,4483	0,4500	0,4493
H2 [mm]	0,7530	0,7489	0,7488	0,7515	0,7488	0,7516	0,7486	0,7502	0,7480	0,7500

H3 [mm]	1,4749	1,4766	1,4747	1,4745	1,4805	1,4784	1,4771	1,4767	1,4790	1,4729
H4 [mm]	2,9934	3,0028	3,0020	3,0026	2,9972	3,0015	2,9964	2,9994	3,0040	3,0025
No of points	$7{,}0 \times 10^5$	$6{,}9 \times 10^5$	$7{,}1 \times 10^5$	$6{,}4 \times 10^5$	$6{,}5 \times 10^5$	$7{,}0 \times 10^5$	$7{,}0 \times 10^5$	$6{,}8 \times 10^5$		$2{,}9 \times 10^6$

Tab.5: Measurement errors of the coaxial cylinders with respect to the certified dimensions and comparison with the errors of the manual scale method.

Errors [μm]	pos 1	pos 2	pos 3	pos 4	pos 5	pos 6	pos 7	Average	Std. Dev.	ABS MAX	Av. Manual [43]
PES D1	4,6	0,3	3,5	-1,8	ND	0,7	0,1	1,2	ND	4,6	-2,5
PES D2	-2,7	-3,2	-0,8	ND	ND	-5,2	ND	-3,0	ND	5,2	-7,3
PES D3	-0,3	-0,5	0,4	ND	ND	-2,6	-0,6	-0,7	ND	2,6	1,9
PES D4	-0,2	4,0	0,6	3,9	-23,8	-1,0	-1,1	-2,5	9,6	23,8	0,9
UPSE H1	-1,9	-0,2	-1,0	-3,9	-1,9	-2,1	-0,9	-1,7	1,2	3,9	-0,7
UPSE H2	5,0	0,9	0,8	3,5	0,8	3,6	0,6	2,2	1,8	5,0	2,0
UPSE H3	-4,1	-2,4	-4,3	-4,5	1,5	-0,6	-1,9	-2,3	2,2	4,5	-3,2
UPSE H4	-10,6	-1,2	-2,0	-1,4	-6,8	-2,5	-7,6	-4,6	3,7	10,6	-1,5

Despite that, it is possible to see that the *PES* of each cylinders is lower than 3μm and in the worse than manual scale method of *1,6μm* for the diameter of the *cylinder 4* only. The measures of the heights show an improvement of the estimate of the *cylinder 3* of 0,9μm, instead for *cylinders 1*, *2* e *4* we have a downturn in *1μm*, *0,2μm e 3,1μm* respectively.

The slight downturn in results could be associated at the order of the number of the points, that is 10^5, differently on the number of the point of the manual scale method that in on the order of 10^6.

REFERENCES

[1] E. Uhlmann, B. Mullany, D. Biermann, K. P. Rajurkar, T. Hausotte, and E. Brinksmeier, “Process chains for high-precision components with micro-scale features,” *CIRP Ann. - Manuf. Technol.*, vol. 65, no. 2, pp. 549–572, 2016.

[2] E. Savio, L. De Chiffre, and R. Schmitt, “Metrology of freeform shaped parts,” *CIRP Ann. - Manuf. Technol.*, vol. 56, no. 2, pp. 810–835, 2007.

[3] A. Gallo, M. Muzzupappa, and F. Bruno, “3D reconstruction of small sized objects from a sequence of multi-focused images,” *J. Cult. Herit.*, vol. 15, no. 2, pp. 173–182, 2014.

[4] T. Brajlih, T. Tasic, I. Drstvensek, B. Valentan, M. Hadzistevic, V. Pogacar, J. Balic, and B. Acko, “Possibilities of Using Three-Dimensional Optical Scanning in Complex Geometrical Inspection,” *Strojniški Vestn. – J. Mech. Eng.*, vol. 57, no. 11, pp. 826–833, 2011.

[5] A. Robinson, M. McCarthy, S. Brown, A. Evenden, and L. Zou, “Improving the Quality of Measurements through the Implementation of Customised Standards,” *Proc. 3rd Int. Conf. 3D Body Scanning Technol. Lugano, Switzerland, 16-17 Oct. 2012*, no. October, pp. 235–246, 2012.

[6] G. Percoco and A. J. Sánchez Salmerón, “Photogrammetric measurement of 3D freeform millimetre-sized objects with micro features: an experimental validation of the close-range camera calibration model for narrow angles of view,” *Meas. Sci. Technol.*, vol. 26, no. 9, p. 95203, 2015.

[7] L. M. Galantucci, M. Pesce, and F. Lavecchia, “A powerful scanning methodology for 3D measurements of small parts with complex surfaces and sub millimeter-sized features, based on close range photogrammetry,” *Precis. Eng.*, 2015.

[8] G. Percoco, F. Lavecchia, and A. J. S. Salmeron, “Preliminary study on the 3D digitization of millimeter scale products by means of photogrammetry,” *Procedia CIRP*, vol. 33, pp. 257–262, 2015.

[9] K. Atsushi, H. Sueyasu, Y. Funayama, and T. Maekawa, “System for reconstruction of three-dimensional micro objects from multiple photographic images,” *CAD Comput. Aided Des.*, vol. 43, no. 8, pp. 1045–1055, 2011.

[10] D. Sims-Waterhouse, S. Piano, and R. Leach, “Verification of micro-scale photogrammetry for smooth three-dimensional object measurement,” *Meas. Sci. Technol.*, vol. 28, no. 5, p. 55010, 2017.

[11] D. Sims-Waterhouse, P. Bointon, S. Piano, and R. K. Leach, “Experimental comparison of photogrammetry for additive manufactured parts with and without laser speckle projection,” in *Proceedings of SPIE - The International Society for Optical Engineering*, 2017, vol. 10329.

[12] D. Sims-Waterhouse, P. Bointon, S. Piano, and R. K. Leach, “Experimental comparison of photogrammetry for additive manufactured parts with and without laser speckle projection,” 2017, vol. 10329, p. 103290W.

[13] G. Percoco, M. G. Guerra, A. J. Sanchez Salmeron, and L. M. Galantucci, “Experimental investigation on camera calibration for 3D photogrammetric scanning of micro-features for micrometric resolution,” *Int. J. Adv. Manuf. Technol.*, vol. 91, no. 9–12, pp. 2935–2947, Aug. 2017.

[14] F. Lavecchia, M. G. Guerra, and L. M. Galantucci, “The influence of software algorithms on photogrammetric micro-feature measurement’s uncertainty,” *Int. J. Adv. Manuf. Technol.*, pp. 1–15, Aug. 2017.

[15] M. Laasonen, “Recognition of Building Parts From Measured Data,” *Measurement*, 2005.

[16] W. T. Estler, K. L. Edmundson, G. N. Peggs, and D. H. Parker, “Large-Scale Metrology – An Update,” vol. 1, no. 2.

[17] M. Fiani, F. Menna, and S. Troisi, “Integrazione di tecniche di fotogrammetria e laser scanning per la modellazione 3d della carena di una imbarcazione,” pp. 173–173.

[18] A. H. Ahmadabadian, S. Robson, J. Boehm, M. Shortis, K. Wenzel, and D. Fritsch, “A comparison of dense matching algorithms for scaled surface reconstruction using stereo camera rigs,” *ISPRS J. Photogramm. Remote Sens.*, vol. 78, pp. 157–167, 2013.

[19] L. Klein, N. Li, and B. Becerik-Gerber, “Imaged-based verification of as-built documentation of

operational buildings," *Autom. Constr.*, vol. 21, no. 1, pp. 161–171, 2012.
[20] H. González-Jorge, B. Riveiro, P. Arias, and J. Armesto, "Photogrammetry and laser scanner technology applied to length measurements in car testing laboratories," *Meas. J. Int. Meas. Confed.*, vol. 45, no. 3, pp. 354–363, 2012.
[21] T. Luhmann, "Close range photogrammetry for industrial applications," *ISPRS J. Photogramm. Remote Sens.*, vol. 65, no. 6, pp. 558–569, 2010.
[22] M. A. Abbas, H. Setan, Z. Majid, A. K. Chong, and D. D. Lichti, "Improvement in measurement accuracy for hybrid scanner," *IOP Conf. Ser. Earth Environ. Sci.*, vol. 18, p. 12066, 2014.
[23] I. Toschi, E. Nocerino, M. Hess, F. Menna, B. Sargeant, L. Macdonald, F. Remondino, and S. Robson, "Improving automated 3D reconstruction methods via vision metrology," no. i.
[24] R. Jiang, D. V. Jáuregui, and K. R. White, "Close-range photogrammetry applications in bridge measurement: Literature review," *Meas. J. Int. Meas. Confed.*, vol. 41, no. 8, pp. 823–834, 2008.
[25] G. G. M. Russo, F. Remondino, "PRINCIPALI TECNICHE E STRUMENTI PER IL RILIEVO TRIDIMENSIONALE IN AMBITO ARCHEOLOGICO," pp. 337–363, 2011.
[26] G. Percoco, F. Modica, and S. Fanelli, "Image analysis for 3D micro-features: A new hybrid measurement method," *Precis. Eng.*, vol. 48, 2017.
[27] Cultural Heritage Imaging, "Guidelines for Calibrated Scale Bar Placement and Processing," pp. 1–11, 2015.
[28] Agisoft LLC, "Agisoft PhotoScan User Manual," p. 37, 2011.
[29] V. Der, "Vdi / Vde 2634," pp. 1–20, 2011.
[30] S. Pertuz, D. Puig, and M. A. Garcia, "Analysis of focus measure operators for shape-from-focus," *Pattern Recognit.*, vol. 46, no. 5, 2013.
[31] J. Lorenzo, M. Castrillón, J. Méndez, and O. Déniz, "Exploring the use of local binary patterns as focus measure," in *2008 International Conference on Computational Intelligence for Modelling Control and Automation, CIMCA 2008*, 2008.
[32] X. Yi and M. Eramian, "LBP-Based Segmentation of Defocus Blur," *IEEE Trans. Image Process.*, vol. 25, no. 4, pp. 1626–1638, Apr. 2016.
[33] N. Otsu, "A Threshold Selection Method from Gray-Level Histograms," *IEEE Trans. Syst. Man. Cybern.*, vol. 9, no. 1, pp. 62–66, Jan. 1979.
[34] T. Ojala, M. Pietikäinen, and D. Harwood, "A comparative study of texture measures with classification based on featured distributions," *Pattern Recognit.*, vol. 29, no. 1, pp. 51–59, Jan. 1996.
[35] P. Viola and M. Jones, "Rapid object detection using a boosted cascade of simple features," in *Proceedings of the 2001 IEEE Computer Society Conference on Computer Vision and Pattern Recognition. CVPR 2001*, vol. 1, p. I-511-I-518.
[36] M. Heikkila and M. Pietikainen, "A texture-based method for modeling the background and detecting moving objects," *IEEE Trans. Pattern Anal. Mach. Intell.*, vol. 28, no. 4, pp. 657–662, Apr. 2006.
[37] T. Ojala, M. Pietikainen, and T. Maenpaa, "Multiresolution gray-scale and rotation invariant texture classification with local binary patterns," *IEEE Trans. Pattern Anal. Mach. Intell.*, vol. 24, no. 7, pp. 971–987, Jul. 2002.
[38] A. Levin, D. Lischinski, and Y. Weiss, "A Closed-Form Solution to Natural Image Matting," *IEEE Trans. Pattern Anal. Mach. Intell.*, vol. 30, no. 2, pp. 228–242, Feb. 2008.
[39] H. Lei, H. Xie, W. Zou, X. Sun, K. Kpalma, and N. Komodakis, "Hierarchical saliency detection via probabilistic object boundaries," *Int. J. Pattern Recognit. Artif. Intell.*, vol. 31, no. 6, 2017.
[40] J. Shi, L. Xu, and J. Jia, "Discriminative Blur Detection Features," in *2014 IEEE Conference on Computer Vision and Pattern Recognition*, 2014, pp. 2965–2972.
[41] K. Murphy, Y. Weiss, and M. I. Jordan, "Loopy Belief Propagation for Approximate Inference: An Empirical Study," Jan. 2013.
[42] C. R. Maurer, Rensheng Qi, and V. Raghavan, "A linear time algorithm for computing exact Euclidean distance transforms of binary images in arbitrary dimensions," *IEEE Trans. Pattern Anal. Mach. Intell.*, vol. 25, no. 2, pp. 265–270, Feb. 2003.
[43] G. Percoco, F. Modica, and S. Fanelli, "Image analysis for 3D micro-features: A new hybrid measurement method," *Precis. Eng.*, 2017.